Numerical Simulation of the Heat Transfer from a Heated Solid Wall to an Impinging Swirling Jet

Joaquín Ortega-Casanova

Área de Mecánica de Fluidos, ETS de Ingeniería Industrial, C/ Dr. Ortiz Ramos s/n,
Universidad de Málaga, 29071 Málaga
Spain

1. Introduction

Swirling jets are frequently used in many industrial applications such as those related with propulsion, cleaning, combustion, excavation and, of course, with heat transfer (e.g. cooling/heating), among others. The azimuthal motion is usually given to the jet by different mechanisms, being the most used by means of nozzles with guided-blades (e.g. Harvey, 1962); by entering the fluid radially to the device (e.g. Gallaire et al., 2004); by the rotation of some solid parts of the device (e.g. Escudier et al., 1980); or by inserting helical pieces inside a cylindrical tube (e.g. Lee et al., 2002), among other configurations. The way the swirl is given to the flow will finally depend on the particular application it will be used for.

Impinging swirling (or not swirling) jets against heated solid walls have been extensively used as a tool to transfer heat from the wall to the jet. In the literature, one can find many works that study this kind of heat transfer related problem from a theoretical, experimental or numerical point of view, being the last two techniques presented in many papers during the last decade. In that sense, Sagot et al. (2008) study the non-swirling jet impingement heat transfer problem from a flat plate, when its temperature is constant, both numerically and experimentally to obtain an average Nusselt number correlation as a function of 4 non-dimensional parameters. And, what is most important from a numerical point of view, their numerical results, obtained with the commercial code Fluent© and the Shear Stress Transport (SST) $k - \omega$ turbulence model for values of Reynolds number (*Re*) ranging from 10E3 to 30E3, agree very well with previous experimental results obtained by Fenot et al. (2005), Lee et al. (2002) and Baughn et al. (1991).

More experimental results are given by O'Donovan & Murray (2007), who studied the impinging of non-swirling jets, and by Bakirci et al. (2007), about the impinging of a swirling jet, against a solid wall. The last ones visualize the temperature distribution on the wall and evaluate the heat transfer rate. In Bakirci et al. (2007), the swirl is given to the jet by means of a helical solid insert with four narrow slots machined on its surface and located inside a tube. The swirl angle of the slots can be varied in order to have jets with different swirl intensity levels. This is a commonly extended way of giving swirl to impinging jets in heat transfer applications, as can be seen in Huang & El-Genk (1998), Lee et al. (2002), Wen & Jang (2003) or Ianiro et al. (2010). On the other hand, Angioletti et al. (2005), and for Reynolds numbers ranging between 1E3 and 4E3, present turbulent numerical simulations of the impingement of a non-swirling jet against a solid wall. Their results are later validated by Particle Image

Velocimetry (PIV) experimental data: when the Reynolds number is small, their numerical results, obtained with the SST $k - \omega$ turbulence model, fit very well the experimental data, while for high Reynolds number values, either the Re-Normalization Group (RNG) $k - \epsilon$ model or the Reynolds Stress Model (RSM) works better. Others previous numerical studies, as the ones by Akansu (2006) and by Olson et al. (2004), show that the SST $k - \omega$ turbulence model is able to predict very well the turbulence in the near-wall region in comparison with other turbulence models. This fact is essential to obtain accurately the turbulent heat transfer from the wall.

Another different turbulent model, presented by Durbin (1991), is used by Behnia et al. (1998; 1999) to predict numerically the heat transfer from a flat solid plate by means of turbulent impinging jets, showing their results good agreement with experimental data. The inconvenient of this last turbulent model is that it does not come originally with Fluent package, so it is ruled out as an available turbulent model.

The work presented here in this chapter deals with the numerical study about the heat transfer from a flat uniform solid surface at a constant temperature to a turbulent swirling jet that impinges against it. To that end, the commercial code Fluent© is used with the corresponding turbulent model and boundary conditions. As any turbulent numerical study where jets are involved, it needs as boundary condition the velocity and turbulence intensity profiles of the jet, and the ones measured experimentally, by means of a Laser Doppler Anemometry (LDA) technique, at the exit of a swirl generator nozzle will be used. The nozzle, experimental measurements and some fitting of the experimental data will be shown in Section 2. Different information, about the computational tasks and decisions taken, will be presented in Section 3, such as those related with the computational domain, its discretization, the numerical methods and boundary conditions used and the grid convergence study. After that, in Section 4 the different results obtained from the numerical simulations will be presented and discussed. They will be divided into two subsections: one to see the effect of varying the Reynolds number; and another to see the effect of increasing or decreasing the nozzle-to-plate distance. Finally, the document will conclude with Section 5, where a summary of the main conclusions will be presented together with some recommendations one should take into account to enhance the heat transfer from a flat plate when a turbulent swirling jet impinges against it.

2. Experimental considerations

Regarding the experimental swirling jet generation, it is created by a nozzle where the swirl is given to the flow by means of swirl blades with adjustable angles located at the bottom of the nozzle (see Fig. 1). After the fluid moves through the blades, it finally exits the nozzle as a swirling jet. Due to the fact that blades can be mounted with five different angles, swirling jets with different swirl intensities can be generated. Thus, for a given flow rate, or Reynolds number (defined below), through the nozzle, five different swirling jets with five different swirl intensities, or swirl numbers (defined below), can be obtained. When the blades are mounted radially, no swirl is imparted to the jet and the swirl number will be practically zero. This blade configuration will be referred in what follows as R. However, with the blades rotated the maximum possible angle, the jet will have the highest swirl levels (and then the highest swirl numbers). This configuration will be referred as $S2$. Between R and $S2$ configurations there are other 3 possible blade orientations, but only the one with the most tangential orientation, $S2$, will be considered in this work. Fig. 2 shows a 2-D view of the
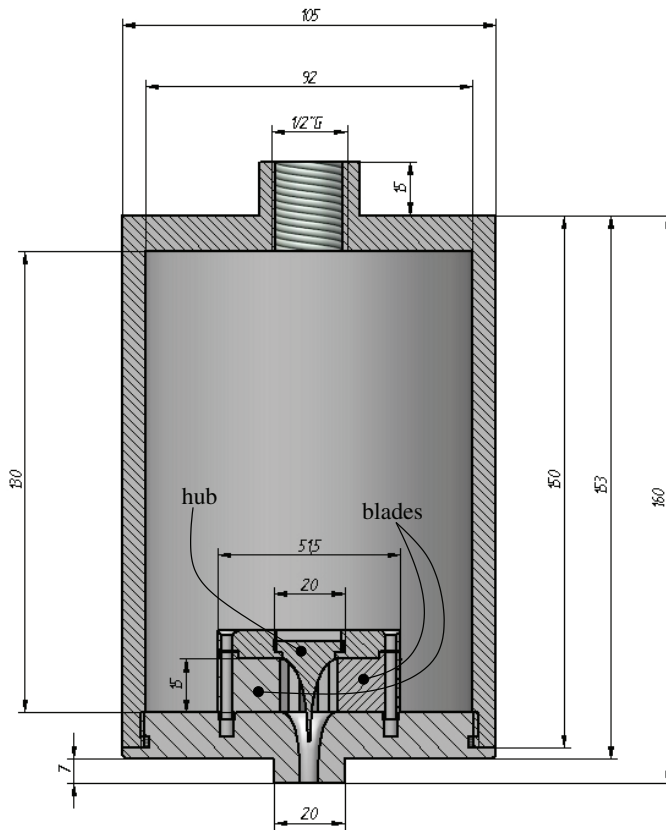
Fig. 1. 2D view of the nozzle. The dimensions are in mm.

swirl blades mounted radially and with the most tangential angle, *R* and *S*2 configuration, respectively.

Similar devices to the one used here to generate the swirling jet are commonly used in several industrial applications, but its use in this work is motivated by two reasons: firstly, by seabed excavation devices that usually use a swirl component to enhance their excavation performance (see Redding, 2002), instead of using a totally axial jet; and secondly, to compare the heat transfer performance of the impinging swirling jet with that obtained experimentally by the same kind of impinging swirling jets but under seabed excavation tasks and reported in Ortega-Casanova et al. (2011). They show that better results (in terms of the size of the scour created) are obtained when the swirl blades are rotated the maximum possible angle, *S*2 configuration, and for the highest nozzle-to-plate distance studied. Thus, the objective of this numerical study is to be able to answer the question about whether or not the *S*2 configuration and the largest nozzle-to-plate distance, also give the highest heat transfer from the plate to the jet.

To model the swirling turbulent jet created by the nozzle is necessary to know both the average velocity field and its turbulent structure at the exit nozzle. In a cylindrical coordinate system
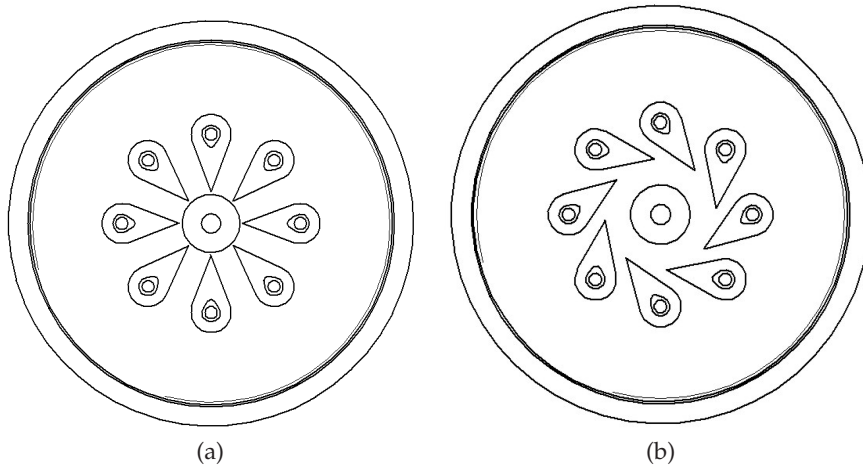
(a)   (b)

Fig. 2. 2D view of the guided blades: mounted radially, R configuration, (a); and rotated the maximum angle, $S2$ configuration, (b).

(r, θ, z), the mean velocity components of the velocity vector will be indicated by $\vec{V}(r, \theta, z) = (U, V, W)$, while the jet turbulence will be take into account by the velocity fluctuations, $\vec{v}'(r, \theta, z) = (u', v', w')$. Both vectors have been previously measured experimentally by means of a LDA system and, due to the shape of the exit tube of the nozzle (see Fig. 1), the radial component of both $\vec{V}$ and $\vec{v}'$ has been considered small enough to be neglected: $U = 0 = u'$. Typical non-dimensional mean velocity profiles at the nozzle exit, together with its fluctuations, are shown in Fig. 3 for two flow rates, the smallest and the highest used, $Q \approx 100$ l/h and $Q \approx 270$ l/h, respectively. In the same figure is also included, with a solid line, the fitting of the experimental data (see Ortega-Casanova et al., 2011, for more details about the fitting models used). In Fig. 3, the velocity has been made dimensionless using the mean velocity W_c based on the flow rate through the nozzle, $W_c = 4Q/(\pi D^2)$, and the radial coordinate with the radius of the nozzle exit $D/2$.

In addition, Fig. 3 shows that, for a given blade orientation, $S2$ in our case, the swirl intensity of the jet will depend on the flow rate Q through the nozzle, since the azimuthal velocity profile is different depending on Q, too. Due to this, the one and only non-dimensional parameter governing the kind of jet at the nozzle exit is the Reynolds number:

$$Re = \frac{\rho W_c D}{\mu} = \frac{4\rho Q}{\mu \pi D},\tag{1}$$

where ρ and μ are the density and viscosity of the fluid, respectively: in Ortega-Casanova et al. (2011) the flow rate ranges from 100 l/h to 270 l/h, so the Reynolds number ranges from 7E3 to 18.3E3, approximately. On the other hand, once the blade orientation is given, $S2$ [shown Fig. 2(b)], the swirl intensity of the jet will depend only on the Reynolds number, and following Chigier et al. (1967), an integral swirl number S_i can be defined to quantify the swirl intensity of the jet as

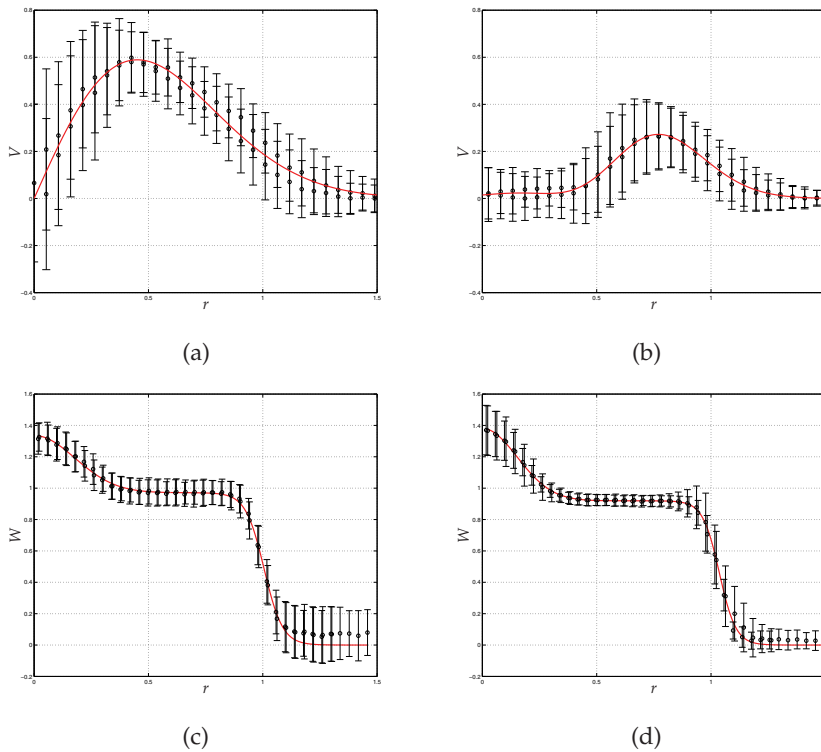$$S_i = \frac{\int_0^\infty r^2 WV \, dr}{(D/2) \int_0^\infty r \left(W^2 - \frac{1}{2}V^2 \right) \, dr}.\tag{2}$$

Fig. 3. Dimensionless azimuthal, (a) and (b), and axial, (c) and (d), velocity profiles for $S2$ configuration. $Q \approx 100 \, \mathrm{l/h}$ for (a) and (c); and $Q \approx 270 \, \mathrm{l/h}$ for (b) and (d). The circles indicate mean velocity values and the error bars its fluctuations.

The evolution of S_i versus the Reynolds number for the blade orientation under study is shown in Fig. 4.

As it has been pointed out previously, the swirl intensity of the jet S_i will depend on the blade orientation and the flow rate. As can be seen in Fig. 4, $S2$ configuration produces jets with variable levels of swirl, with its maximum around $Re \approx 9\mathrm{E}3$. This Reynolds number divides the curve in two parts: the left one, $Re \lesssim 9\mathrm{E}3$, in which S_i increases with Re; and the right one, $Re \gtrsim 9\mathrm{E}3$, in which S_i decreases with Re. S_i has been calculated using (2) and the non-dimensional mean axial and azimuthal velocity profiles measured just downstream of the nozzle exit. Both components of the velocity are depicted in Fig. 5 for all Reynolds numbers experimentally studied. From this figure can easily be understood the behavior of S_i for $S2$ configuration. These profiles are also shown in Ortega-Casanova et al. (2011), but are reproduced here again in order to have a complete and general idea of the swirling jets generated by the nozzle configuration under study. When the swirl increases with the rotation of the blades, not only the dimensional azimuthal velocity increases, as it was expected, but also the maximum axial velocity at the axis, appearing a well defined overshoot around it (see the axial and azimuthal velocity profiles for other blade orientations in Ortega-Casanova et al., 2011). In addition to this, another effect associated with the increasing of the blade rotation
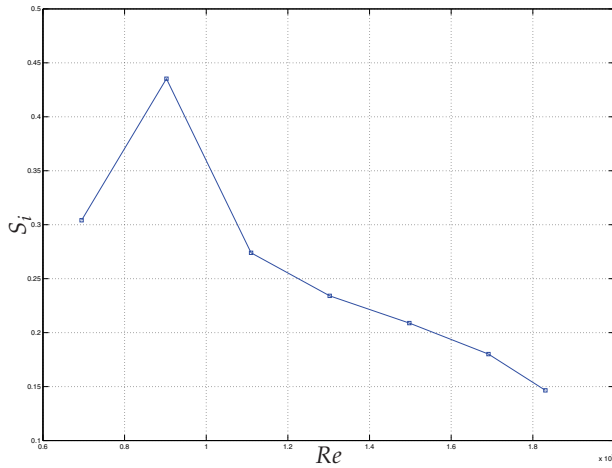
Fig. 4. Integral swirl number S_i as a function of the Reynolds number. $S2$ configuration.

is the appearance of a swirless region near the axis and a shift of all the azimuthal motion to a region off the axis when the Reynolds number is above a certain value, as can be seen in Fig. 5(a) for $Re > 11E3$. This swirless region has nothing to do with vortex breakdown since the axial velocity [Fig. 5(b)] does not have any characteristic of this phenomena, like a reverse flow at the axis with a stagnation point at a certain radius of the profile. This phenomena has been recently observed experimentally by Alekseenko et al. (2007), where vortex breakdown occurs for jet swirl intensities above a critical value (see, e.g., Lucca-Negro & O'Doherty, 2001, for a recent review about that phenomena).

Also, in Ortega-Casanova et al. (2011) is shown that the best combination for excavation purposes in order to produce deeper and wider scours on sand beach is the axial overshoot together with the shift of the azimuthal motion to an annular region. They also discuss and give the mathematical models that better fit the experimental data, shown also in Fig. 3 with solid lines. Obviously, when $S2$ configuration is used, as it is here, the azimuthal velocity models depend on the Reynolds number considered, being different the one used for low Reynolds numbers ($Re \leq 11E3$) than for high ones ($Re \geq 13E3$).

Those models will be used now as a boundary condition to specify the velocity components of the swirling jet in the numerical simulations. However, not only the model of the velocity profiles are needed to model the turbulent jet, but also is necessary to model its turbulence. Once the velocity fluctuations $\vec{v}'$ have been measured, the turbulent intensity I of the jet can be estimated as

$$I = \frac{\sqrt{u'^2 + v'^2 + w'^2}}{W_c} \simeq \frac{\sqrt{v'^2 + w'^2}}{W_c}. \tag{3}$$

In order to have an analytical function of the turbulent intensity profile to be used as boundary condition, all turbulent intensity I profiles must be fitted and it is found that the best fitting is achieved with the Gaussian model
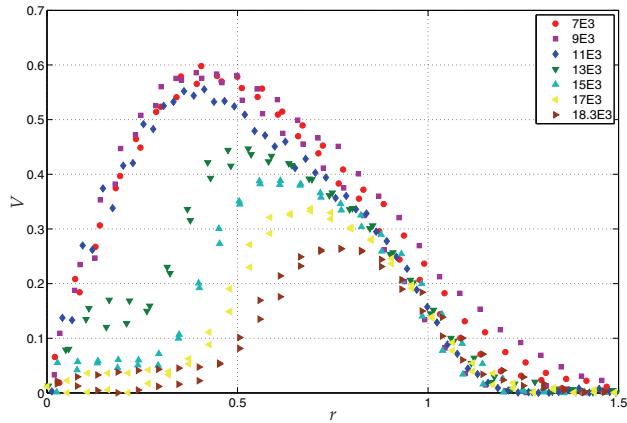
(a)
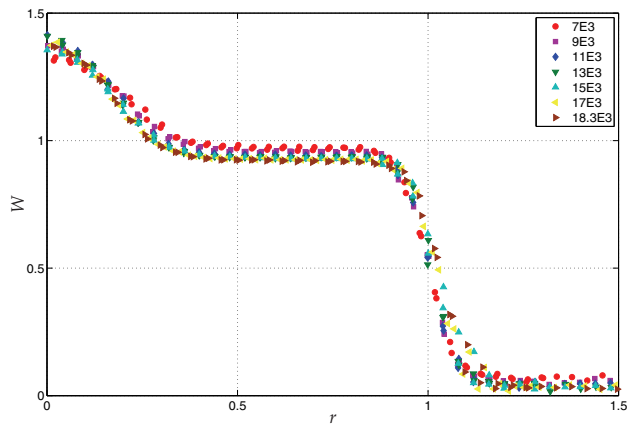
(b)

Fig. 5. Mean dimensionless azimuthal (a) and axial (b) velocities measured just downstream the nozzle exit.

$$I = \sum_{i=1}^{n} a_i e^{\left[-\left(\frac{r - b_i}{c_i} \right)^2 \right]}, \tag{4}$$

where r is the dimensionless radial coordinate and a_i, b_i and c_i are fitting parameters depending on the Reynolds number. It has been checked that $n = 3$ is enough to fit quite well, and with the simplest model, the radial I profile for any value of Re. Fig. 6 shows the profile of I for two values of the Reynolds number. For low Re and almost all radial positions, the swirling jet is more turbulent than for high Re, with the highest levels of turbulence around the axis, while for high Re, the turbulence is more uniform. The profiles shown in Fig. 6
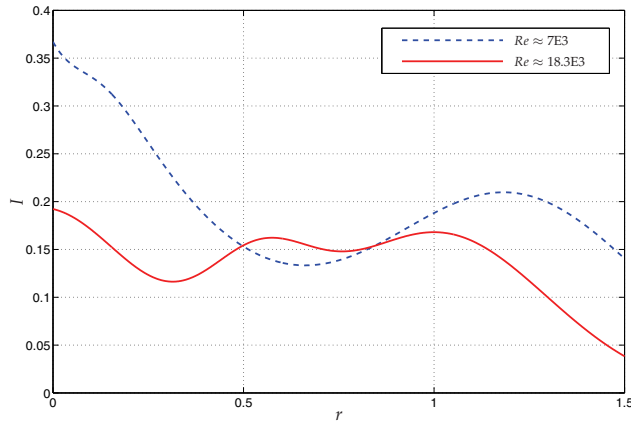
Fig. 6. Turbulent intensity radial distribution when the Reynolds numbers are the indicated in the legend.

has been obtained with (3) and the velocity fluctuations shown in Fig. 3. Once this turbulent magnitude has been fitted, it will be used later to specify the appropriate boundary conditions in the turbulent model used (see next section).

The turbulent swirling jets measured experimentally at the nozzle exit by means of a LDA system are ready to be used as boundary condition in the numerical simulations thank the models of both azimuthal and axial velocity components as well as the one of the turbulent intensity.

3. Computational considerations

The numerical simulations have been carried out by means of the commercial code Fluent© (version 6.2.16). As for any numerical turbulent simulations, some previous things must be chosen, such as the turbulent model, the optimum grid, the computational geometry and boundary conditions, etc.

Firstly, the computational geometry together with the corresponding boundary conditions used will be presented. The problem is considered to be axisymmetric, so only a 2D $r - z$ section of the three-dimensional geometry will be solved. Fig. 7 shows a sketch of the heat transfer problem solved in this work together with the different boundary conditions used: the swirl generator nozzle is located at a distance H above the solid hot plate (whose radius is $\mathcal{R}$) where the swirling jet will impinge once it leaves the nozzle as a swirling jet (the non-dimensional nozzle-to-plate distance will be indicated by the ratio H/D); once the impinging takes place, the fluid leaves the computational domain through either the side or top surface. The velocity and turbulent intensity profiles shown in the previous section will be introduced into the simulations by a ``velocity inlet´´ boundary condition at the left-top of the domain by means of a User Defined Function (abbreviated as UDF in what follows) in order to model the nozzle above the plate. As can be seen in Fig. 7, the nozzle exit is surrounded by an annular solid part of the nozzle. It will be modeled giving to the velocity components in that region an almost zero value through the velocity profile at the ``velocity inlet´´ boundary

Numerical Simulation of the Heat Transfer from
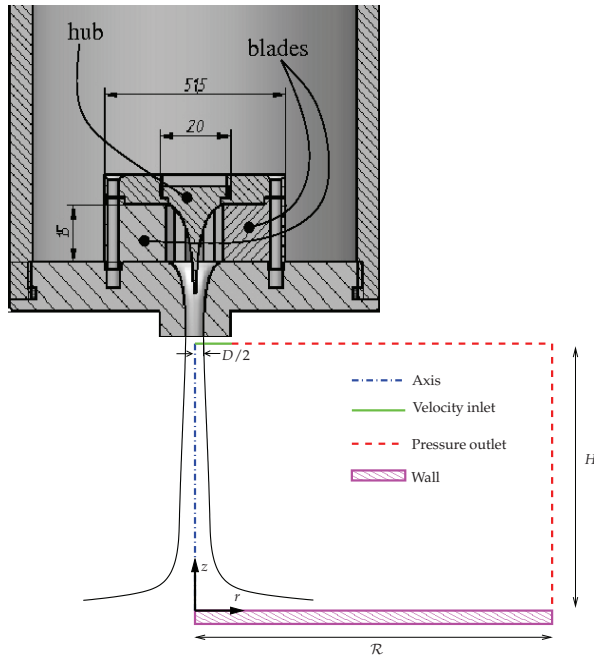a Heated Solid Wall to an Impinging Swirling Jet
181

Fig. 7. Sketch of the computation domain. The nozzle and type of boundary condition used are also included.

condition. However, Fluent does not allow to specify a turbulent intensity distribution or profile but a constant value. Due to this, in order to indicate the turbulent structure of the swirling jet when it leaves the swirl generator nozzle by the measurements taken experimentally, the turbulent intensity I must be turned into other turbulent magnitudes that will depend on the turbulent model used, as it will be shown later. The surfaces where the fluid is allowed to leave the computational domain (the right and top side) will be indicated as ``pressure-outlet´´ boundary conditions. The bottom of the geometry represents the solid hot plate where the fluid will impinge and is considered as a no-slip surface with a prescribed temperature and modeled as a ``wall´´ boundary condition (Sagot et al., 2008, showed that almost similar results can be obtained when the boundary condition on the solid plate is either a prescribed temperature or heat flux). Finally, the left line from the nozzle exit to the plate at the bottom will be indicated as an ``axis´´ boundary condition, since it represents the axis of symmetry of the problem.

Regarding the turbulent model, the $k - \omega$ one will be used, in particular, its version SST. This decision is based on the previous works review presented in the Introduction because is the one used by Sagot et al. (2008) (where good agreement between numerical and experimental solutions are shown) and because the Reynolds number used here, in this work, ranges between 7E3 and 18.3E3, close to those employed in Sagot et al. (2008).

The flow we are interested in solving with this problem is considered turbulent, steady and axisymmetric with the fluid (water) having its density constant (incompressible fluid) as in Ortega-Casanova et al. (2011). Thus, the steady Reynolds Averaged Navier-Stokes (RANS)

equations are solved numerically to obtain any fluid magnitude. They can be written in Cartesian tensor notation as:
the continuity equation:

$$\frac{\partial V_i}{\partial x_i} = 0; \tag{5}$$

the momentum equations:

$$\frac{\partial (V_i V_j)}{\partial x_j} =$$

$$-\frac{1}{\rho}\frac{\partial p}{\partial x_i} + \nu \frac{\partial}{\partial x_j}\left[\frac{\partial V_i}{\partial x_j} + \frac{\partial V_j}{\partial x_i} - \frac{2}{3}\delta_{ij}\frac{\partial V_l}{\partial x_l}\right]$$

$$+ \frac{\partial\left(-\overline{v_i' v_j'}\right)}{\partial x_j}; \tag{6}$$

and the energy equation:

$$\frac{\partial}{\partial x_i}\left[V_i(\rho e + p)\right] = \frac{\partial}{\partial x_j}\left[K_{eff}\frac{\partial T}{\partial x_j}\right] \tag{7}$$

with

$$e = h - \frac{p}{\rho} + \frac{\vec{V}\cdot\vec{V}}{2}, \tag{8}$$

where ν is the kinematic viscosity, h is the enthalpy, K is the thermal conductivity and $K_{eff} = K + K_t$ is the effective thermal conductivity that takes into account the turbulent thermal conductivity K_t: $K_t = c_p \mu_t / Pr_t$. c_p is the specific heat, μ_t is the turbulent dynamic viscosity and Pr_t is the turbulent Prandtl number. Also, two closure equations are needed: one to know the turbulent kinetic energy k and another one for the specific turbulent dissipation rate ω:

$$\rho\frac{\partial}{\partial x_i}(kV_i) = \frac{\partial}{\partial x_j}\left(\Gamma_k\frac{\partial k}{\partial x_j}\right) + G_k - Y_k, \tag{9}$$

$$\rho\frac{\partial}{\partial x_i}(\omega V_i) = \frac{\partial}{\partial x_j}\left(\Gamma_\omega\frac{\partial \omega}{\partial x_j}\right) + G_\omega - Y_\omega, \tag{10}$$

where: Γ_k and Γ_ω are the effective diffusivity of k and ω, respectively; G_k and G_ω are the generation of k and ω, respectively, due to mean velocity gradients; and Y_k and Y_ω are the dissipation of k and ω, respectively. To know more about their definition and implementation in Fluent, the reader is remitted to Fluent 6.2 User's Guide (2005).

Regarding the boundary conditions shown in Fig. 7, their implementation in Fluent was as follows:

Axis: since this line is an axis of symmetry, the boundary conditions ``axis ˝ was chosen;

Pressure outlet: both the side and top surfaces were supposed to be at the same constant pressure, so the boundary condition ``pressure-outlet˝ was chosen;

Wall: this surface is considered as a smooth no-slip stationary solid surface at constant temperature T_w, so the boundary condition ``wall˝ was chosen, imposing its temperature at the known constant value.

Velocity inlet: in this surface, the corresponding radial dependence axial and azimuthal velocity profile associated with the corresponding Reynolds number under study was imposed trough an UDF file through a ``velocity-inlet´´ boundary condition. The models used to fit the velocity profiles shown in Fig. 3 are given in Ortega-Casanova et al. (2011), and the reader is remitted there to know more about them. On the other hand, regarding the specification of the swirling jet turbulence levels, the turbulence intensity can be estimated from the LDA measurements, eq. (3), and fitting to a radial profile, eq. (4), but Fluent does not allow to specify as boundary condition a radial dependence profile for the turbulence intensity but a constant value. For that reason, and in order to specify the radial turbulence distribution of the jet, the turbulence intensity is turned into the variables k and ω for which are possible to indicate a radial profile as boundary condition. Once the mean axial and azimuthal velocities are measured, W and V, respectively, together with its fluctuations, w' and v', respectively, and with the turbulent intensity I given by (3), k and ω can be obtained as

$$k = \frac{3}{2} \left(\overline{U} I \right)^2 , \tag{11}$$

$$\omega = \frac{800}{25} \frac{\overline{U} I}{D_H}, \tag{12}$$

where I is in %, $\overline{U} = \sqrt{W^2 + V^2}$, and D_H is the hydraulic diameter of the nozzle exit. While (11) is given by Fluent 6.2 User's Guide (2005), (12) has been obtained numerically giving different values to $\overline{U}$, I and D_H on a velocity inlet boundary condition, and relating the ω value giving by Fluent on that boundary with them [(11) has been also confirmed by the same methodology]. On the other hand, the jet leaves the nozzle at a constant temperature T_j.

The presence of solid surfaces when turbulent flows are solving numerically, needs special attention in order to solve efficiently the boundary layer along the solid surface. This fact is crucial in our problem since there is a solid surface where the swirling jet impinges and the heat transfer from the surface must be solved precisely. This requires that the nearest grid point to the solid hot plate must be as close to the surface as possible to have an $y+$ of unity order. To achieve this, rectangular stretched meshes with different node densities have been generated with the total nodes ranging from 13 000 to 60 000. All meshes have in common that the mesh nodes density is higher near the solid hot plate, the axis, the mixing layer and the nozzle exit. The grid independence study were done with five grids in order to choose from them the optimum one. The number of nodes, with the maximum value of $y+$ along the solid hot plate indicated in parenthesis, used were: 13 041 (8.0); 22 321 (4.0); 30 000 (0.4); 37 901 (0.4) and 60 551 (0.4). The $y+$ values previously indicated were obtained from the numerical simulation of the most unfavorable case studied (see next section): the one with the highest Reynolds number ($Re \approx 18.3E3$), and the shortest nozzle-to-plate distance, i.e. $H/D = 5$. The grid density near the solid hot plate selected as the optimum for this H/D will be reproduced, in that zone, for other nozzle-to-plate distances, or H/D values, that is, the radial node distribution and the one next to the plate along axial direction: meshes for different values of H/D will differ only on the axial node distribution and the number of nodes along that direction.

The minimum $y+$ obtained in the grid independence process was 0.4, but in 3 different grids, so the optimum will be selected in terms of the area-weighted average Nusselt number along

the solid hot plate. On the one hand, the Nusselt number will be defined as

$$Nu(r, Re) = \frac{q(r)\, D}{K\, \Delta T}\,, \tag{13}$$

where q is the total heat flux from the solid hot wall to the fluid and ΔT is the temperature difference between the wall (T_w) and the swirling jet emerging from the nozzle (T_j). And, on the other hand, the area-weighted average Nusselt number along a surface S is defined as

$$\overline{Nu}(Re) = \frac{1}{S} \int_S Nu(r, Re)\, \mathrm{d}S, \tag{14}$$

which is a measurement of the dimensionless mean heat transferred from the solid hot plate to the jet.

Using the finest grid (60 551 nodes), $\overline{Nu}$ on the solid hot plate only changes $\approx 1\%$ and the computational time increases by 78% with respect to the grid with $\simeq 38\,000$ nodes. For these reasons, the grid chosen as the optimum was the one with $nr \times nz = 37\,901$ nodes (nr and nz are the number of nodes along r and z directions, respectively). Regarding the radial direction, the optimum mesh has $nr = 251$ non uniform nodes compressed around the axis ($r = 0$) and the mixing layer ($r \simeq D/2$). On the other hand, the number of nodes along the axial direction depends on the nozzle-to-plate distance. Thus, for $H/D = 5$, $nz = 151$; for $H/D = 10$, $nz = 201$ and for $H/D = 30$, $nz = 301$. The first node from both the solid hot plate, along the axial direction, and the axis, along the radial direction, is at a distance equal to 0.0025 mm.

To conclude this section, new computational information is added below. A typical simulation requires about 70E3 iterations to converge, detected by the convergence with the iterations of: the equation residuals; a monitor, defined as the area-weighted average Nusselt number on the solid hot plate; and the mass conservation between the inlet and outlets of the computational domain. About one fifth of the total iterations were done using first order methods to discretize the convective terms of the transport equations, while the remaining iterations were done with the second order schemes PRESTO (PREssure STaggering Option) and QUICK (Quadratic Upwind Interpolation for Convective Kinematics). The Pressure-Velocity Coupling were carried out with the SIMPLE (Semi-Implicit Method for Pressure-Linked Equations) scheme. On the other hand, the gravity effects have been not taken into account since the inertial forces are much bigger than the gravitational ones, so that the Froude number is much bigger than one.

4. Results

In this section, the results obtained will be presented, once the heat transfer from the solid hot wall to the impinging swirling jet has been solved numerically. This section will be divided in two subsections dedicated to present the effect of increasing both the nozzle-to-plate distance and the Reynolds number. The results will be discussed in terms of both the Nusselt number $Nu(r, Re)$ and the area-weighted average Nusselt number $\overline{Nu}(Re)$, both calculated on the solid hot plate. Three distances, $H/D = 5, 10$ and 30, and seven Reynolds numbers, $Re \approx 7E3$, 9E3, 11E3, 13E3, 15E3, 17E3 and 18.3E3, have been studied, as in Ortega-Casanova et al. (2011). Previous works related with both heat transfer and impinging jets have focused their attention in distances H/D smaller than 10 (see Brown et al., 2010, for recent results
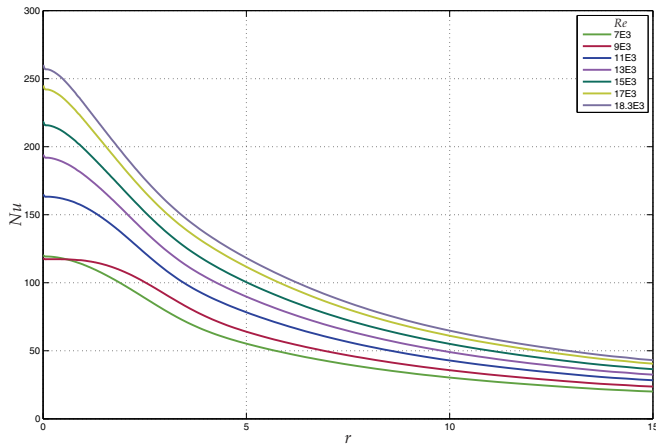
Fig. 8. Nu evolution for $H/D = 5$ and the Re indicated in the legend.
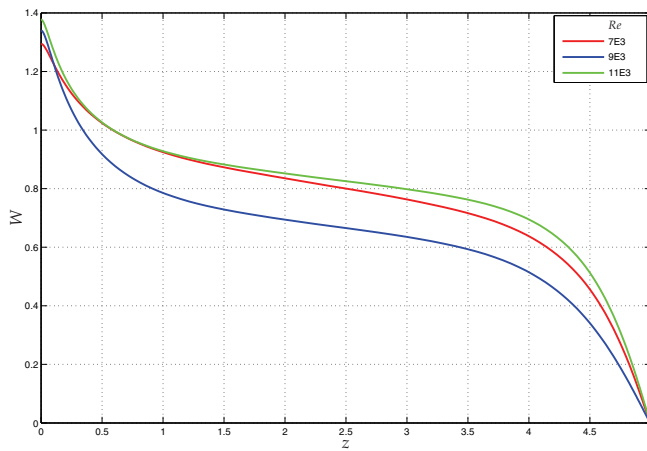

Fig. 9. Evolution of W along the axis: $H/D = 5$ and the Reynolds numbers are indicated in the legend. z has been made dimensionless with D.

when H/D ranges between 0.5 and 10), so that, the behavior for larger distances will be also discussed in this work.

4.1 Effect of Reynolds number.

First of all, it must be remembered that the swirl intensity of each jet is different according with Fig. 4, and that its value will be important in order to explain how Nusselt number on the solid hot plate changes with Reynolds number.

In Fig. 8 is plotted the evolution of Nu along the solid hot plate for the different Reynolds numbers studied and the smaller nozzle-to-plate distance, $H/D = 5$. For this smallest distance, when Re increases, Nu increases for any radial position, except for $Re \approx$ 9E3, the one with the highest S_i (see Fig. 4), for which there exists a small region around the axis where Nu is smaller than the one for $Re \approx$ 7E3. Therefore, the jet with the highest S_i, the one corresponding to $Re \approx$ 9E3, produces a more uniform region around the axis where Nu is almost constant, being at the stagnation point $r = 0$ slightly smaller than that of the previous and smaller Reynolds number.

The above mentioned uniform Nu region near the axis when $Re \approx$ 9E3 is due to the high swirl intensity of the jet for which a deceleration of the vortex along the axis occurs, without appearing its breakdown, that would require higher swirl intensity levels to appear, as it does in Alekseenko et al. (2007), where the vortex breakdown of a turbulent impinging swirling jet is observed experimentally above a critical jet swirl intensity. In order to explain the previously commented deceleration of the swirling jet, in Fig. 9 is depicted the axial evolution of the dimensionless axial velocity along the axis for three Reynolds numbers. One can observe how the jet with the highest S_i produces a slower jet along the axis than the other two. Probably, swirling jets with $S_i \gtrsim 0.45$ could finally undergo breakdown downstream the swirl generator nozzle but they have not been obtained experimentally with the $S2$ configuration. For this small nozzle-to-plate distance, it must be noted an imperceptible decreasing of the Nusselt number in the region near to the axis, close to the stagnation point, thing that happens for all Reynolds numbers.

When the nozzle-to-plate distance is doubled, i.e. $H/D = 10$, things are quite similar. Fig. 10 shows the radial evolution of Nu along the solid hot plate when the different jets impinged against it. The main difference with respect to the previous and smaller separation is that the swirl intensity of the jet when $Re \approx$ 9E3 is not big enough to decelerate the jet along the axis in order to produce a more uniform Nu number region than for $Re \approx$ 7E3: the higher the nozzle-to-plate distance, the higher the S_i needed to decelerate the flow around the axis in order to reach the vortex breakdown conditions. This was also shown in Ortega-Casanova et al. (2008), where the impingement of a family of swirling jets against a solid wall were studied numerically: higher swirl intensity levels were needed to observe vortex breakdown when the separation of the impinged plate increased. Therefore, since there is not enough deceleration of the jet, always that Re increases, Nu increases, too, for any radial coordinate (see Fig. 10). On the other hand, comparing Fig. 8 and 10, one can also observe that the Nusselt number at the stagnation point decreases when the separation increases.

When the nozzle-to-plate distance is the highest studied, the behavior is the same than for $H/D = 10$: increasing Re, the corresponding swirling jet produces a higher Nu distribution at any radial position than lower Reynolds number jets, but Nu levels are lower in comparison with smaller nozzle-to-plate distances. Therefore, the increasing of the separation between the nozzle and the solid hot plate will produce lower heat transfer from the plate to the jet at any radial location on the plate, assuming a constant Re. This comment can be seen clearly at the stagnation point $r = 0$ if the Nusselt number there is plotted against the Reynolds number for the different distances studied, as it is shown in Fig. 12(a). On the other hand, if one takes into account the area-weighted average Nusselt number, given in (13), on the solid hot plate and is plotted versus the Reynolds number, as it is done in Fig. 12(b), one can see that $\overline{Nu}$ increases almost linearly with Re for small nozzle-to-plate distances, $H/D = 5, 10$, while for the highest distance studied, $H/D = 30$, the tend is nonlinear for the highest Reynolds numbers. From
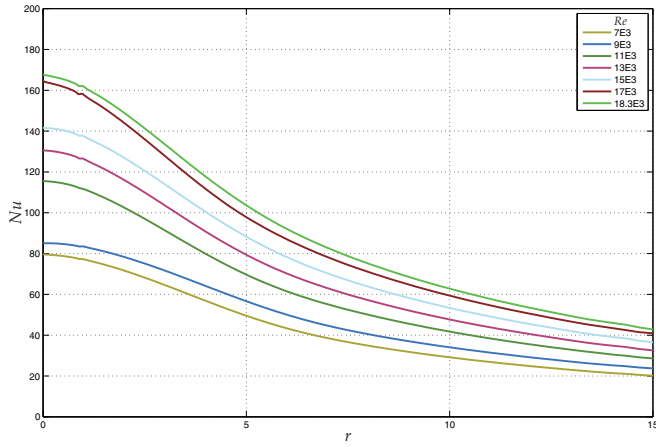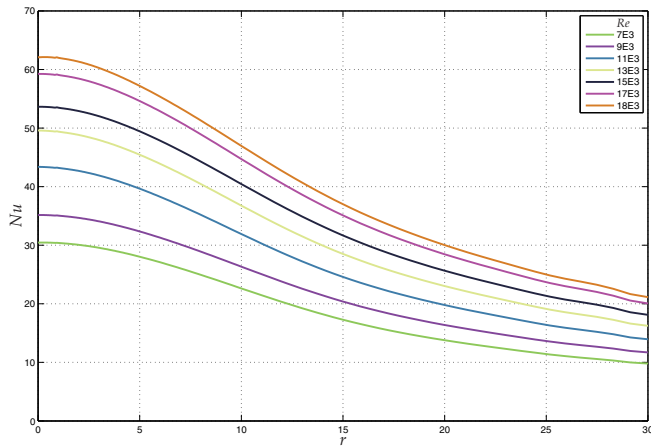
Fig. 10. As in Fig. 8, but for $H/D = 10$.

Fig. 11. As in Fig. 8, but for $H/D = 30$.

this last figure, it could be interesting to know how $\overline{Nu}$ changes with Re in comparison with $\overline{Nu}(7\mathrm{E}3)$, that is, the ratio given by

$$\frac{\overline{Nu}(Re)}{\overline{Nu}(7\mathrm{E}3)} \equiv \overline{Nu}_{7\mathrm{E}3}^{Re}. \tag{15}$$

This function is depicted in Fig. 13: for $H/D = 5, 10$, $\overline{Nu}_{7\mathrm{E}3}^{Re}$ is almost the same and linearly varying with Re; however, when $H/D = 30$ the evolution is nonlinear, being remarkable what happens for high Reynolds numbers, in comparison with the other smaller values of H/D.
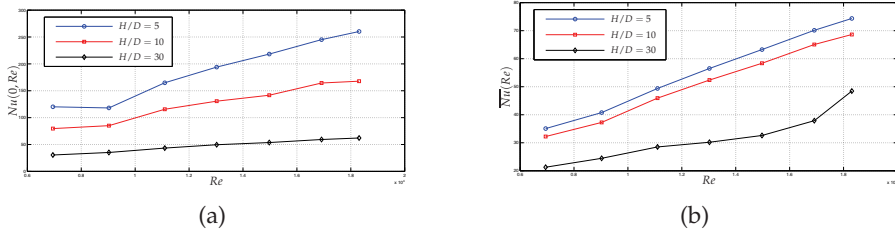
(a)

(b)

Fig. 12. Evolution of: (a) $Nu(0, Re)$; and (b) $\overline{Nu}(Re)$. The corresponding value of H/D is indicated in the legend.
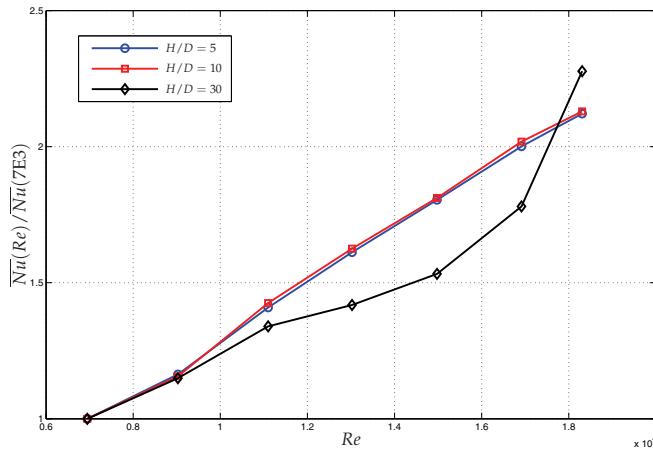

Fig. 13. Evolution of $\overline{Nu}_{7E3}^{Re}$ for the values of H/D given in the legend.

From these curves, very different predictions are obtained if they are extrapolated to higher Reynolds numbers than the ones studied. Consequently, the benefits of using the highest Reynolds number swirling jet, generated by the $S2$ configuration, to transfer heat from an impinged solid hot plate to the jet, are higher than using the low/medium Reynolds number ones when the distance between the nozzle and the plate is the highest possible: from Fig. 13 can easily be seen that for $H/D = 5, 10$, $\overline{Nu}(18.3E3) \simeq 2.1 \times \overline{Nu}(7E3)$, while for $H/D = 30$ this ratio is a little bit higher, that is, $\overline{Nu}(18.3E3) \simeq 2.3 \times \overline{Nu}(7E3)$. If one takes a look at Fig. 5(a), the previously commented facts could be explained in a different way: the effect of the displacement of the azimuthal velocity to an annular region off the axis, appearing at high Reynolds numbers, has more influence in the heat transfer at high distances between the nozzle and the solid hot plate.

4.2 Effect of the nozzle-to-plate distance.

When Reynolds number is considered constant, the effect of increasing the nozzle-to-plate distance gives as result a quick decreasing of the heat transfer from the solid hot plate to the impinging jet. The decreasing rate is higher at high Reynolds numbers than at low ones, as
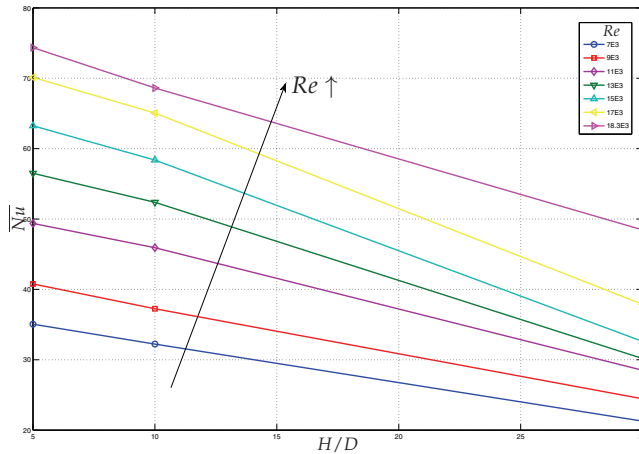
Fig. 14. Evolution of $\overline{Nu}$ for the constant values of Re indicated in the legend.

can be seen in Fig. 14, where the evolution of $\overline{Nu}$ for each Re studied is shown versus the nozzle-to-plate distance: for a given Reynolds number, the heat transfer always decreases when the separation increases; the decreasing will be higher or lower depending on the corresponding value of Re.

5. Conclusion

In this work, numerical simulations of the impingement of a turbulent swirling jet against a solid hot plate at constant temperature have been presented. The jet has been modeled by experimental measurements taken by means of a LDA equipment at the exit of a nozzle that imparts the swirl to the jet by guided blades, and with the jet swirl intensity depending only on the Reynolds number. Seven Reynolds numbers and three nozzle-to-plate distances have been simulated, which gives a total of 21 numerical simulations. The analysis of the results gives the following conclusions:

Firstly, taken into account that the main objective of this work was to see if the performance of the heat transfer was higher for the highest nozzle-to-plate distance than for lower ones, as in Ortega-Casanova et al. (2011) under seabed excavation tasks, it must be said that the question is answered negatively: the heat transfer from the solid hot plate to the impinging swirling jet always decreases when the separation increases, at least for the type of jets used here. Therefore, the sand, that is, the granular media used in Ortega-Casanova et al. (2011) on which the swirling jet impinged, plays an important role in reaching the scour its final shape, especially when $H/D = 30$ and the highest Reynolds number jets are used. For that combination, the impinging swirling jet creates the deepest and widest scours. When the same swirling jet impinges against undeformable solid surfaces, the qualitative results, in term of the heat transferred from the surface, are totally different from those obtained when the impingement takes place against granular media and cannot be extrapolated from excavation related problems to heat transfer ones, and vice versa.

Secondly, the area-weighted average Nusselt number on the solid hot plate, always increases with Reynolds number and for any value of the nozzle-to-plate distance, i.e. for any H/D. Almost the same happens with the Nusselt evaluated at the stagnation point $r = 0$: only for $Re \approx 9E3$ and $H/D = 5$, this is not true due to the combination of the highest jet swirl intensity and the smallest nozzle-to-plate distance, for which a deceleration of the swirling jet takes place but without being high enough for the vortex breakdown to be observed. The effect of the deceleration was not to increase the Nusselt number at the stagnation point but to create a more uniform Nu region around the axis. Despite that decreasing in the stagnation point Nusselt number, the mean heat transfer, i.e. $\overline{Nu}$, on the surface always increases with Re. On the other hand, for high nozzle-to-plate distances, the benefits of using high Reynolds number jets instead of low ones, are higher than at small nozzle-to-plate distances. This fact has much to do with the displacement of the azimuthal motion of the swirling jet to an annular region off the axis that has more influence on the heat transferred from the solid hot plate when the nozzle-to-plate is the highest studied. The above mentioned displacement of the azimuthal motion takes place for Reynolds numbers greater than 13E3, approximately. It could have been interesting to study the heat transfer when the solid hot wall is impinged with swirling jets that have undergone breakdown and to compare the Nusselt distributions on the solid hot wall due to the impingement of swirling jets with and without breakdown. Unfortunately, vortex breakdown has not been observed experimentally with the nozzle configuration and flow rates used in this work.

And finally, the area-weighted average Nusselt number always decreases with the increasing of the nozzle-to-plate distance: for a given Reynolds number, the smaller the nozzle-to-plate distance, the higher the heat transferred from the plate to the jet.

6. Acknowledgement

7. References

Akansu, S. O. (2006). Heat transfers and pressure drops for porous-ring turbulators in a circular pipe. *Applied Energy*, 83, 280-298.

Alekseenko, S. V.; Bilsky, A. V.; Dulin V. M. & Markovich, D. M. (2007). Experimental study of a impinging jet with different swirl rates. *International Journal of Heat and Fluid Flow*, 28, 1340-1359.

Angioletti, M.; Nino, E. & Ruocco, G. (2005). CFD turbulent modeling of jet impingement and its validation by particle image velocimetry and mass transfer measurements. *International Journal of Thermal Sciences*, 44, 349-356.

Bakirci, K. & Bilen, K. (2007). Visualization of heat transfer for impinging swirl flow. *Experimental Thermal and Fluid Science*, 32, 182-191.

Baughn, J. W.; Hechanova, A. E. & Yan, X. (1991). An experimental study of entrainment effect on the heat transfer from a flat surface to a heated circular impinging jet. *Journal of Heat Transfer*, 113, 1023-1025.

Behnia, M.; Parneix, S. & Durbin, P. A. (1998). Prediction of heat transfer in an axisymmetric turbulent jet impinging on a flat plate. *International Journal of Heat and Mass Transfer*, 41, 1845-1855.

Behnia, M.; Parneix, S.; Shabany, Y. & Durbin, P. A. (1999). Numerical study of turbulent heat transfer in confined and unconfined impinging jets. *International Journal of Heat and Fluid Flow*, 20, 1-9.

Brown, K. J.; Persoons, T. & Murray, D. B. (2010). Heat transfer characteristics of swirling impinging jets. *In Proceedings of the 14th International Heat Transfer Conference, IHTC14*. pp 14. Washington, DC, USA. August 8-13, 2010. Edited by ASME, New York.

Chigier, N. A. & Chervinsky, A. (1967). Experimental investigation of swirling vortex motion in jets. *Journal of Applied Mechanics*, 34, 443-451.

Durbin, P. 1991. Near-wall turbulence closure without damping functions. *Theoretical and Computational Fluid Dynamics*, 3, 1-13.

Escudier, M. P.; Bornstein, J. & Zehnder, N. 1980. Observations and LDA measurements of confined turbulent vortex flow. *Journal of Fluid Mechanics*, 98, 49-63.

Fenot, M.; Vullierme, J.-J.; & Dorignac, E. (2005). Local heat transfer due to several configurations of circular air jets impinging on a flat plate with and without semi-confinement. *International Journal of Thermal Sciences*, 44, 665-675.

Fluent 6.2 user's guide (2005). Fluent Incorporated, Centerra Resource Park, 10, Cavendish Court, Lebanon (NH) 03766 USA.

Gallaire, F.; Rott, S. & Chomaz, J. M. (2004). Experimental study of a free and forced swirling jet. *Physics of Fluids*, 16, 2907-2917.

Harvey, J. K. (1962). Some observations of the vortex breakdown phenomenon. *Journal of Fluid Mechanics*, 14, 585-592.

Huang, L. & El-Genk, M. S. (1998). Heat transfer and flow visualization experiments of swirling, multi-channel, and conventional impinging jets. *International Journal of Heat and Mass Transfer*, 41, 583-600.

Ianiro, A.; Cardone, G. & Carlomagno, G. M. (2010). Convective Heat-Transfer in swirling Impinging jets. Book of Papers of the 5th International Conference on Vortex Flow and Vortex Methods. ISBN: 978-88-905218-6-7. 8-10 November, Caserta (Italy).

Lee, D. H.; Won, S. Y.; Kim, Y. T. & Chung, Y.S. (2002). Turbulent heat transfer from a flat surface to a swirling round impinging jet. *International Journal of Heat and Mass Transfer*, 45, 223-227.

Lucca-Negro, O. & O'Doherty, T. (2001). Vortex breakdown: a review. Progress in Energy and Combustion Science, 27, 431-481.

O'Donovan, T. S. & Murray, D. B. (2007). Jet impingement heat transfer - Part I: Mean and root-mean-square heat transfer and velocity distributions. *International Journal of Heat and Mass Transfer*, 50, 3291-3301.

Olsson, E. E. M.; Ahrné, L. M. & Trägardh, A. C. (2004). Heat transfer from a slot air jet impinging on a circular cylinder. *Journal of Food Engineering*, 63, 393-401.

Ortega-Casanova, J.; Martín-Rivas, S. & del Pino, C. (2008). Estudio numérico del impacto de un chorro con giro, turbulento y axilsimétrico contra una superficie sólida (in Spanish). In *Nolineal 2008, edited by F. Marqués and A. Delshams*. pp. 101. ISBN: 978-84-96739-48-1. CIMNE. Barcelona.

Ortega-Casanova, J.; Campos, N. & Fernandez-Feria, R. (2011). Experimental study on sand bed excavation by impinging swirling jet. Submitted to the *Journal of Hydraulic Research* (accepted for publication).

Redding, J. H. (2002). The SILT X-Cavator: technical aspects and modes of operation. In: Dredging' 02: Key Technology for Global Prosperity. Orlando.

Sagot, B.; Antonini, G.; Christgen, A. & Buron, F. (2008). Jet impingement heat transfer on a flat plate at a constant wall temperature. *International Journal of Thermal Sciences*, 47, 1610-1619.

Wen, M. Y. & Jang, K. J. (2003). An impingement cooling on a flat surface by using circular jet with longitudinal swirling strips. *International Journal of Heat and Mass Transfer*, 46, 4657-4667.